Spatially Dense Velocity Structure Exploration in the Source Region of the Iwate-Miyagi Nairiku Earthquake

Masumi Yamada[1], Masayuki Yamada[2], Koji Hada[2], Shiro Ohmi[3], and Takashi Nagao[4]
masumi@eqh.dpri.kyoto-u.ac.jp

1 Introduction

The 2008 Iwate-Miyagi Nairiku earthquake (M_w 6.9, M_{jma} 7.2) occurred in southwestern Iwate prefecture, Japan (39.03°N, 140.88°E, depth 8 km) on June 13, at 23:43:45 GMT (Japan Meteorological Agency, 2008). The surface accelerometer of KiK-net station IWTH25, located 3 km southwest of the epicenter, produced one of the largest strong-motion values of peak ground acceleration (PGA) ever recorded (4278 cm/s^2 for the vector sum of the three components), (KiK-net, 2000), and exhibited an asymmetric amplification in the vertical component (Aoi et al., 2008). This asymmetric amplification has been interpreted to be a result of separation of the surface layer (Aoi et al., 2008; Yamada et al., 2009b). Subjected to extremely strong vertical ground motions, a near-surface soil layer is separated from a sublayer and the motion of the separated layer is controlled by the gravity load (Eisler and Chilton, 1964). When this layer returns, striking the separation surface, high acceleration in the positive direction is produced (Yamada et al., 2009b). However, according to the field reconnaissance (Yamada et al., 2009a), there is no obvious physical evidence of layer separation, and the effects of the local soil properties are not yet clear.

A velocity profile obtained from the logging at the station IWTH25 has been obtained by the National Research Institute for Earth Science and Disaster Prevention (NIED) (see Figure 1). However, transfer functions of the observed ground motions suggest that a slower seismic velocity model than that obtained from the logging data may be appropriate (Yamada et al., 2010). We have conducted spatially dense microtremor array measurements in the area surrounding station IWTH25. The objective of this paper is to estimate the shallow velocity structure around the station

[1]Pioneering Research Unit for Next Generation, Kyoto University, Gokasho, Uji, 611-0011, Japan
[2]NEWJEC Inc., 2-3-20 Honjo-Higashi, Kita-ku, Osaka, 531-0074, Japan
[3]Disaster Prevention Research Institute, Kyoto University, Gokasho, Uji, 611-0011, Japan
[4]National Institute for Land, Infrastructure Management, 3-1-1, Nagase, Yokosuka, 239-0826, Japan

using the microtremor measurements and to provide the information on the spatial variation of the sub-surface velocity structure which is related to the surface layer separation.

2 Data

We performed microtremor measurements around station IWTH25 from May 10 to May 13, 2009, about 11 months after the 2008 Iwate-Miyagi Nairiku earthquake. We used 17 three-component seismometers with flat responses to acceleration between 0.2 and 40 Hz. Four seismometers were the GPL-6A3P model (made by Mitutoyo Corporation); three seismometers a combination of JEP-6A3 sensors (made by Mitutoyo Corporation) and DATAMARK LS-7000XT loggers (made by Hakusan Corporation); and the remaining 10 seismometers combinations of JA-40GA04 sensors (made by Japan Aviation Electronics Industry, Ltd.) and DATAMARK LS-7000XT loggers. The data were recorded at a sampling rate of 100 samples per second.

The target area is a three-level river terrace located next to the Iwai River (see Figure 2). The lowest terrace is an athletic field (hereafter referred to as 'field level'). The middle terrace, 7 m above the field level, is the surface on which the KiK-net station is located (hereafter referred to as 'station level'). The highest terrace is a parking lot which is 12 m above the field level (hereafter referred to as 'parking level'). These heights have been measured by laser surveying.

The site plan of the station is shown in Figure 3. The site encompasses are small concrete structures, a toilet and a septic tank, located in front of the seismic station. The vicinities of these structures ($<$ 1m) may be affected by their foundations.

2.1 Microtremor Measurements

In order to determine spatial variations in the velocity structure, microtremor measurements were obtained at 1-2 m intervals at the station level. The surveyed area was 44 m wide and 20 m long, and contained 395 measurement points (see Figure 3). The area close to the station was surveyed at 1 m spacing, and the other side of the terrace at 2 m spacing.

Each recording was of 660 seconds duration, and the observed accelerograms have been filtered with a fourth-order Butterworth filter using a corner frequency of 0.1 Hz to remove the instrument response. Five segments containing 4096 sampling points were randomly selected from each waveform. A linear taper with a 1 s window was applied to both ends of these time series, the fast Fourier transform (FFT) calculated for each component, and the amplitude spectra smoothed using a Parzen window of 0.2 Hz bandwidth. This filter was found to provide satisfactory smoothing without suppressing significant features in the spectrum. The horizontal component was computed as a geometric mean of the NS and EW amplitude spectra, and H/V spectral ratios were then cal-

culated from the ratio of the horizontal to vertical amplitude spectra. We use geometric mean of two components to take an average in the logarithmic scale. We made 100 selections of 5 segments from each waveform and focused on the set of segments with the smallest standard deviation of the H/V spectra.

The H/V spectra of microtremors at five different sites along line 15 in Figure 3 are shown in Figure 4. The largest peak of the spectra is at 2.7 Hz, which reflects a strong velocity contrast at 34 m depth. These spectra are very stable for frequencies of less than 6 Hz, but show large variances for higher frequency ranges.

2.2 Microtremor Array Measurements

We measured microtremors in a circular array at the parking, station, and field levels. The array sizes are shown in Table 1. For arrays of radius less than 10 m, the sensors were arranged at the center and four corners of the square contained within the circle. For arrays of larger radius, the sensors were arranged at the center and three corners of the triangle contained within the circle. The array configurations are shown in Figures 2 and 3. Each recording was of 900 seconds duration, and the same filtering process as for the microtremor measurements was applied. For each record, 15 data segments containing 2048 sampling points each were selected for analysis.

3 Analysis

3.1 Estimation of Spatial Variation of Velocity Structure

The spatial variation of the H/V spectra is shown in Figure 5. First, the medians of each H/V spectrum at certain frequency bands were computed. The frequency bands used here are 2-4, 4-8 and 8-12 Hz. For each band, a contour map of the median of the H/V spectra was produced.

Figure 5 (a) shows relatively homogeneous H/V amplitudes in the 2-4 Hz band. This frequency band contains the reflection from the strong velocity contrast at 34 m depth. Therefore, the depth of this contrast is assumed to be the same for all sites. Figures 5 (b) and (c) show larger amplitudes in the lower half of the mapped area. These larger amplitudes are considered to be the result of leveling of the ground. Figure 6 shows a cross-section around the station IWTH25 before and after ground leveling was carried out in 1995. In order to level the ground, soil on the uphill side (where the seismic station is located) was moved to the downhill side. The downhill side has accordingly been raised by 1 - 2 m. We assume that this leveling caused the larger response at the high frequencies on the downhill side.

Based on the assumption that the spatial anomaly in Figure 5 (a) was caused by the distur-

bance during the measurement, Figures 5 (d)-(f) show contour maps of the median of the H/V spectra normalized by the median at 2-4 Hz. The upper-left corner of 5 (f) also shows somewhat larger response. These large amplitudes may affect the large acceleration observed during the main shock, but we cannot clearly distinguish special features peculiar to the site around the seismic station. Note that measurements around the white boxes in the left side of each figure may have been affected by the septic tank (especially along line 3). This septic tank was repaired just two weeks before we obtained our measurements, so the H/V spectra at these sites may have been overestimated in this study.

Figure 7 shows the spatial variation of the H/V spectra in the NW-SE (uphill-downhill) direction and the SW-NE (left-right) direction, respectively. The highest peak at 2.7 Hz is consistent across all sites, but the H/V spectra at higher frequencies show spatial variability. For example, Figure 7 shows that the H/V spectrum at 5-10 Hz is larger on the uphill side, and gradually becomes smaller as it moves to the downhill side. Spatial variation in the SW-NE (left-right) direction is not as obvious as in the NW-SE (uphill-downhill) direction.

3.2 Rayleigh Wave Dispersion Curve

The extended spatial autocorrelation (ESPAC) method (Aki, 1957) (Ling, 1993) has been used to determine the dispersion curves of vertical microtremor records. The ESPAC method yields optimal Bessel functions at each frequency from multiple spatial autocorrelation functions observed over different array sizes and times. Spatial autocorrelation functions for different array sizes at the station level are combined with the ESPAC method and the resulting dispersion curve is shown in Figure 8 using red circles. The effective wavelength is 2-10 times as large as the radius of the array for the spatial autocorrelation method (Arai and Tokimatsu, 2005). In our measurement, the largest radius of the array was 40 m. Assuming the average V_s at the shallow layer is about 500 m/s, 1.25 - 6.25 Hz is the lower bound for the frequency of a theoretically reliable dispersion curve.

We also processed the array microtremor data at the parking level using the same method. The dispersion curve is shown in Figure 8 using black crosses, and the dispersion curve corresponding to the velocity structure of the logging data is illustrated as a broken line. The dispersion curve at the parking level is very similar to that of the logging data, and the phase velocities at 6-8 Hz at the station and parking levels are approximately the same. Furthermore, Figure 6 shows that the original geography slopes, so we assume that the soil structures at the station and parking levels are similar. Therefore, assuming that the velocity structure corresponding to frequencies lower than 7 Hz is not substantially different at the parking and station levels, we connect these curves at 7 Hz. We use the combined dispersion curve to invert for S-wave velocity structure at frequencies of 3-30 Hz.

3.3 Estimation of Velocity Structure

3.3.1 Genetic Algorithm Inversion

In Figure 8, the Rayleigh-wave dispersion curve computed from the velocity structure provided by NIED is shown as a dashed line. The dispersion curve is larger than that corresponding to the observed data for frequencies greater than 10 Hz, so the S-wave velocity in the shallow layers may be slower than that obtained from the logging data.

In order to determine a velocity model consistent with the observed dispersion curve, we performed an inversion using a Genetic Algorithm (GA) following Yamanaka and Ishida (1996). The initial model was based on the PS logging data (see Table 2). We split the first layer at 2 m to enable the velocity structure in the shallowest interval to better represent near-surface heterogeneity. The density was computed from the following empirical relationship between P-wave velocity V_p and density ρ (Gardner et al., 1974):

$$\rho[g/cm^3] = 0.31V_p^{0.25}. \tag{1}$$

Sensitivity analyses have shown that the S-wave velocity V_s and thickness of a layer H both have stronger influences than either P-wave velocity or density on Rayleigh wave dispersion curves (e.g. Horike, 1985; Arai and Tokimatsu, 2004), so we fixed ρ at the initial values and defined V_p as a function of V_s (Kitsunezaki et al., 1990):

$$V_p[m/s] = 1.11V_s + 1290. \tag{2}$$

The fitness function (F) we maximize using the GA is the inverse of the residual sum of squares:

$$F = \frac{1}{1/n\sum_{i=0}^{n}[C_o(f_i) - C_e(f_i)]^2}. \tag{3}$$

Here, n is the number of data, $C_o(f_i)$ is the observed dispersion curve, and $C_e(f_i)$ is the estimated dispersion curve at frequency f_i. The search ranges of the parameters were chosen to be $\pm$ 10 % with respect to V_s of the initial model, and $\pm$ 1 m with respect to H of the initial model. The numbers of the populations (individuals) and generations (iterations) for the GA search were 30 and 500, respectively. After 500 iterations, we adopted the optimal model of the run as the initial model for the next run. Using this approach, the search ranges are changed to reflect the new initial model. We produced 30 populations from the model and repeat this process. Even if the optimal model differed significantly from the initial model, or was not included in the initial search ranges, the result was found to approach the optimal model after several repetitions. We repeated the process 10 times to obtain a final model, and the model converged after the final run.

3.3.2 Model Class Selection

Model class selection refers to the process of determining how many parameters should be estimated to identify the optimal velocity model. The deepest two layers have little effect on the dispersion curve at frequencies higher than 3 Hz, so we fix the values of these two layers at the original values. The layer thickness H for all layers and V_s for the bottom 6 layers were fixed at the original values, and the optimum value V_s for the upper 2 layers estimated. We call this model V2H0, which comprises two free variables for V_s. The GA inversion using this model was carried out and the obtained fitness function and optimal values are shown in Table 3. Next, the number of free V_s variables was increased incrementally, and four new models (V3H0, ..., V6H0) constructed. The fitness functions for these models are also shown in Table 3. The V2H0 model has the smallest fitness function, but the other four models all have similar values. We therefore use the Akaike information criterion (AIC) to identify the optimal model.

To use the AIC, it should be assumed that the model errors are normally and independently distributed. We further assume that the variance of the model errors is unknown but equal. Maximizing the likelihood with respect to this variance, the AIC is:

$$AIC = 2k + n[\ln(1/F)]. \tag{4}$$

where k is the number of the free parameters and F is defined in the equation 3. We performed the Levene's test (Zar, 2010) to check the assumption that the variance is equal for all models, and the result shows the assumption is met at the 99% significance level. Therefore, we adopted equation 4 for the model class selection. The computed AIC is shown in the bottom of Table 3. It shows that model V3H0 is the optimal model, which means that changing the velocity at depths below the third layer did not improve the results.

Using the GA process, the values of V_s and H for the top 1 to top 3 layers have been estimated. The fitness function shown in the bottom of Table 3 is similar for all models. Again, we performed the Levene's test to check the equality of the variances, and confirmed that the necessary assumption is met. Then, the AICs for the 3 models were computed. The AIC reveals that the V3H0 model is the optimum one among these four models, so adopted the three variables for V_s, and the fixed H values. The optimal model is shown in Figure 1. The V_s values of the first three layers were each found to be slower than obtained from the logging data. Standard deviations for V_s are also computed from 30 runs of the inversion, and they are less than 2 m/s for all V_s.

4 Discussion and Conclusions

The contour maps of the H/V spectra (Figure 5) exhibit spatial variations in the high-frequency range. The H/V spectra for all sites have their largest peaks around 2.7 Hz, which reflects the strong velocity contrast at 34 m depth. Therefore, the depth of this contrast is concluded to be the same for all sites. The H/V amplitudes of the high-frequency range (medians of 4-8 Hz and 8-12 Hz) are affected by shallow subsurface structures, and the uphill-side spectra show larger amplitudes than those on the downhill side. The H/V spectra around station IWTH25 are somewhat larger than those in the uphill-side area, but they are about the same levels as on the downhill side.

The inferred separation of the subsurface layer during the strong seismic shaking is presumed to be related to the soil conditions. For example, separation needs accelerations larger than 1g, and high-frequency ground motion tends to be amplified at hard rock sites. However, based on our measurements, it is difficult to relate the local soil conditions to the triggering conditions of subsurface layer separation during strong shaking.

The velocity structure determined from the Rayleigh wave dispersion curve shows that S-wave velocities in the shallow layers which are slower than obtained with logging data, are required to explain the observed data. The optimal model has 10-50 % slower S-wave velocities for layers shallower than 34 m, whereas layers deeper than 34 m have the same V_s as found for logging data. Note that this difference may include nonlinear effect of subsurface structure due to the strong shaking. The optimal model exhibits large velocity contrasts at 6 m and 34 m depth. We expect that separation of the layers tends to happen at strong velocity contrasts, but in this case we could not determine which layers were involved.

This study addressed spatial variations in subsurface soil structure and estimated S-wave velocity structure based on microtremor array measurements. Conventional microtremor array measurements have been used for analysis of large-scale soil structure (i.e. several hundred meters to kilometers) but we showed that this methodology is effective to detect the small-scale spatial variation. The results suggest that spatial heterogeneity of H/V spectra in the high-frequency range may be related to the high accelerations, but we cannot clearly illustrate particular features unique to the site surrounding the seismic station. A large acceleration is likely to have been generated in other parts of the surveyed area. The velocity model estimated from the Rayleigh wave dispersion curve reveals slower S-wave velocities than logging data in the shallow layers, with large contrasts at 6 m and 34 m depths. To determine the depth of separation, we need further waveform analysis and soil structure exploration.

Acknowledgments

We thank Kazuo Yoshida, Yoshinori Fujino, and Tomoyuki Kaizuma at NEWJEC for helping to obtain the field measurements in Iwate. We acknowledge NIED for providing strong-motion records and velocity data. Dr. Suqun Ling at Geo-Analysis Institute Co., Ltd., provided the ESPAC program, and Dr. Masanori Horike provided the program used to compute the Rayleigh wave dispersion curve.We also thank Mr. Toshikatsu Matsuya from the Ichinoseki City Hall for supporting our field measurements and providing specification documents for the target site. We are deeply appreciative of comments provided by the associate editor and reviewers. This research was conducted with the support of Promoting Science and Technology grant from the Ministry of Education, Culture, Sports, Science and Technology of Japan.

References

Aki, K. (1957). Space and time spectra of stationary stochastic waves, with special reference to microtremors. *Bulletin of Earthquake Research Institute*, 35:415–456.

Aoi, S., Kunugi, T., and Fujiwara, H. (2008). Trampoline effect in extreme ground motion. *Science*, 322:727–729.

Arai, H. and Tokimatsu, K. (2004). S-wave velocity profiling by inversion of microtremor h/v spectrum. *Bulletin of the Seismological Society of America*, 94(1):53–63.

Arai, H. and Tokimatsu, K. (2005). S-wave velocity profiling by joint inversion of microtremor dispersion curve and horizontal-to-vertical (h/v) spectrum. *Bulletin of the Seismological Society of America*, 95(5):1766–1778.

Eisler, J. and Chilton, F. (1964). Spalling of the earth's surface by underground nuclear explosions. *Journal of Geophysical Research*, 69:5285–5293.

Gardner, G., Gardner, L., and Gregory, A. (1974). Formation velocity and density – the diagnostic basics for stratigraphic traps. *Geophysics*, 39(6):770–780.

Horike, M. (1985). Inversion of phase velocity of long-period microtremors to the S-wave-velocity structure down to the basement in urbanized areas. *Journal of Physics of the Earth*, 33(2):59–96.

Japan Meteorological Agency (2008). Iwate-Miyagi Nairiku earthquake in 2008 http://www.seisvol.kishou.go.jp/eq/2008_06_14_iwate-miyagi/index.html.

KiK-net (2000). http://www.kik.bosai.go.jp/kik/index_en.shtml.

Kitsunezaki, C., Goto, N., Kobayashi, Y., Ikawa, T., Horike, M., Saito, T., Kurota, T., Yamane, K., and Okuzumi, K. (1990). Estimation of P- and S-wave velocities in deep soil deposits for evaluating ground vibrations in earthquake. *Journal of the Japan Society for Natural Disaster Science*, 9(3):1–17. *(in Japanese with English abstract)*.

Yamada, M., Fukushima, Y., and Suetomi, I. (2009a). Building damage during the 2008 Iwate-Miyagi Nairiku Earthquake. *Bulletin of the Disaster Prevention Research Institute, Kyoto University*. *(in Japanese with English abstract)*.

Yamada, M., Mori, J., and Heaton, T. (2009b). The slapdown phase in high-acceleration records of large earthquakes. *Seismological Research Letters*, 80(4):559.

Yamada, M., Mori, J., and Ohmi, S. (2010). Temporal changes of subsurface velocities during strong shaking as seen from seismic interferometry. *Journal of Geophysical Research*, 115, B03302.

Yamanaka, H. and Ishida, H. (1996). Application of genetic algorithms to an inversion of surface-wave dispersion data. *Bulletin of the Seismological Society of America*, 86(2):436–444.

Zar, J. (2010). Biostatistical analysis. *Prentice Hall*, 154–157.

Figures and Tables

Level	Square array	Triangular array
parking	-	10, 20
station	1, 2, 4, 8	10
field	-	10, 20, 40

Table 1: List of the array radii at the parking, station, and field levels (unit: m).

Layer	V_p (m/s)	V_s (m/s)	ρ (g/cm^3)	H (m)
1	850	430	1.67	2
2	850	430	1.67	4
3	1770	530	2.01	28
4	2310	680	2.15	30
5	2310	1120	2.15	48
6	4010	1780	2.47	64
7	2620	1380	2.22	28
8	3180	1810	2.33	56

Table 2: An initial velocity model based on the PS logging data (KiK-net, 2000). The first layer is split at 2 m, which may have a slower S-wave velocity than the PS logging data.

Initial model		Models							
par.	value	V2H0	V3H0	V4H0	V5H0	V6H0	V3H1	V3H2	V3H3
Vs1	430	134	189	186	180	183	199	138	189
Vs2	430	229	225	225	226	226	225	253	253
Vs3	530	-	459	461	462	460	459	463	464
Vs4	680	-	-	675	681	686	-	-	-
Vs5	1120	-	-	-	1096	1060	-	-	-
Vs6	1780	-	-	-	-	2096	-	-	-
H1	2	-	-	-	-	-	2.3	1.9	2.8
H2	4	-	-	-	-	-	(3.7)	5.0	4.1
H3	28	-	-	-	-	-	-	(27.1)	27.5
H4	30	-	-	-	-	-	-	-	(29.6)
F	0.00003	0.00060	0.00205	0.00206	0.00205	0.00207	0.00204	0.00211	0.00206
AIC	-	-	334	336	338	340	336	337	340

Table 3: Model class selection with AIC. VaHb indicates the model ID, where ‘a’ is the number of parameters representing V_s and ‘b’ is the number of parameters H, respectively. The fitness function (F) and AIC of the models are shown at the bottom.

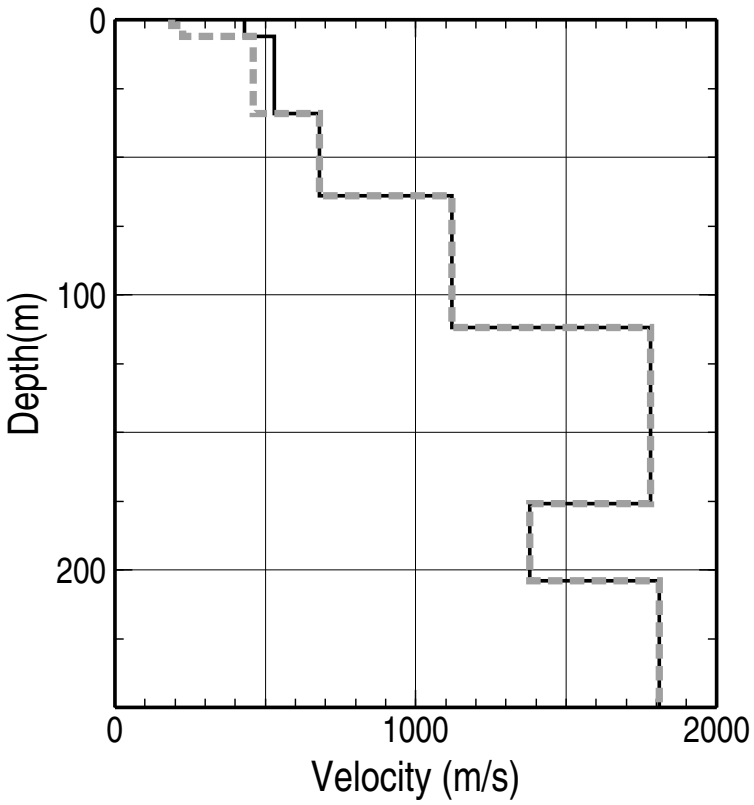

Figure 1: Velocity structure at station IWTH25. The solid line shows the S-wave velocity for the PS logging data, and the dashed line shows the result of the GA inversion. Standard deviations for the result of the GA inversion over 30 runs are; the first layer: 1.73 m/s, the second layer:0.35 m/s, and the third layer: 0.19 m/s.

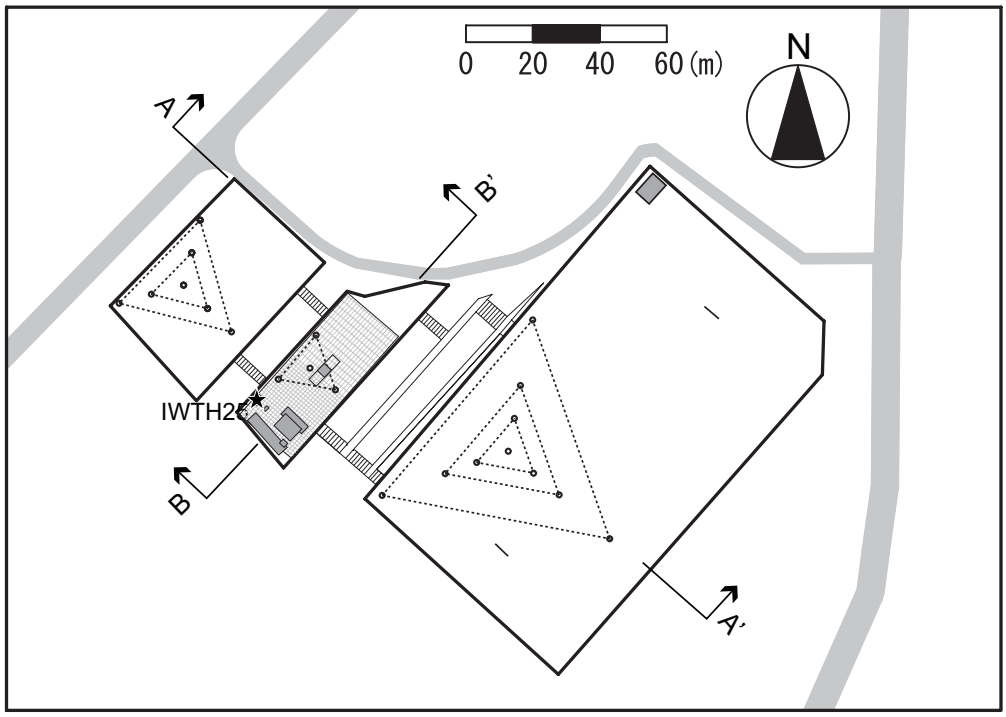

Figure 2: Site plan of station IWTH25. Dashed triangles show the microtremor array configurations.

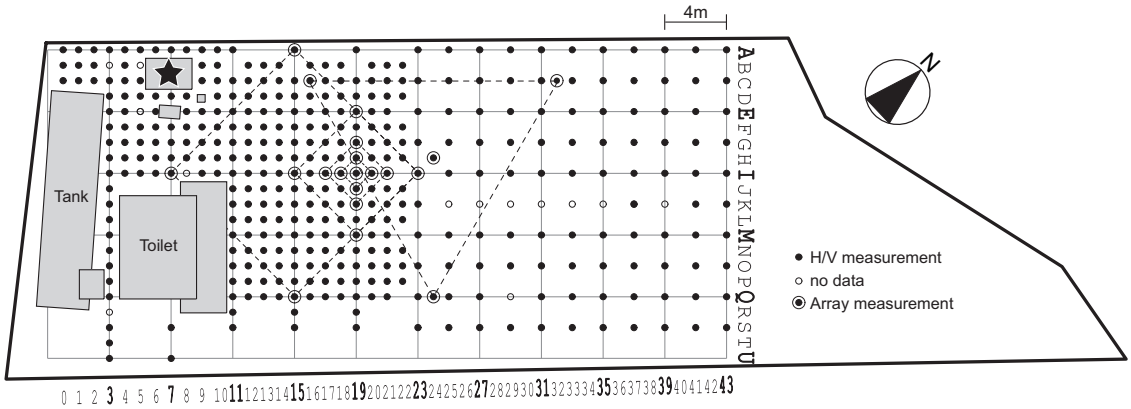

Figure 3: Arrangement of the H/V measurement locations and array measurement locations at the station level. The star shows station IWTH25.

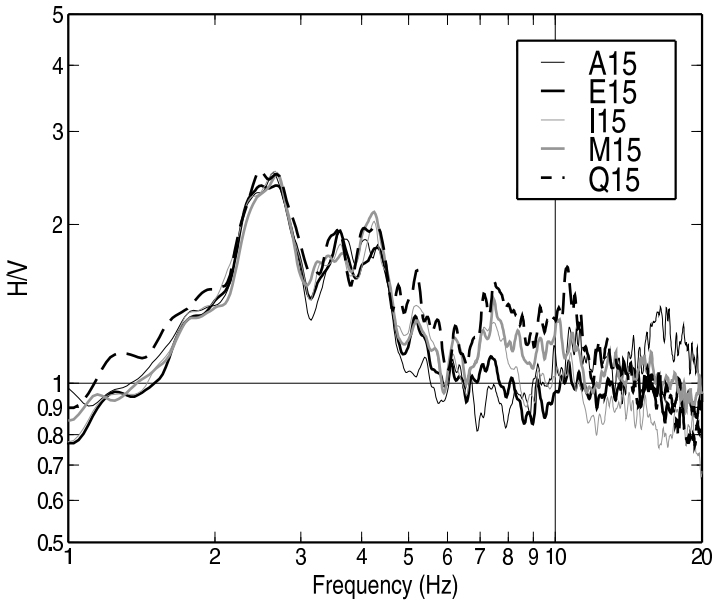

Figure 4: Examples of H/V spectra along line 15.

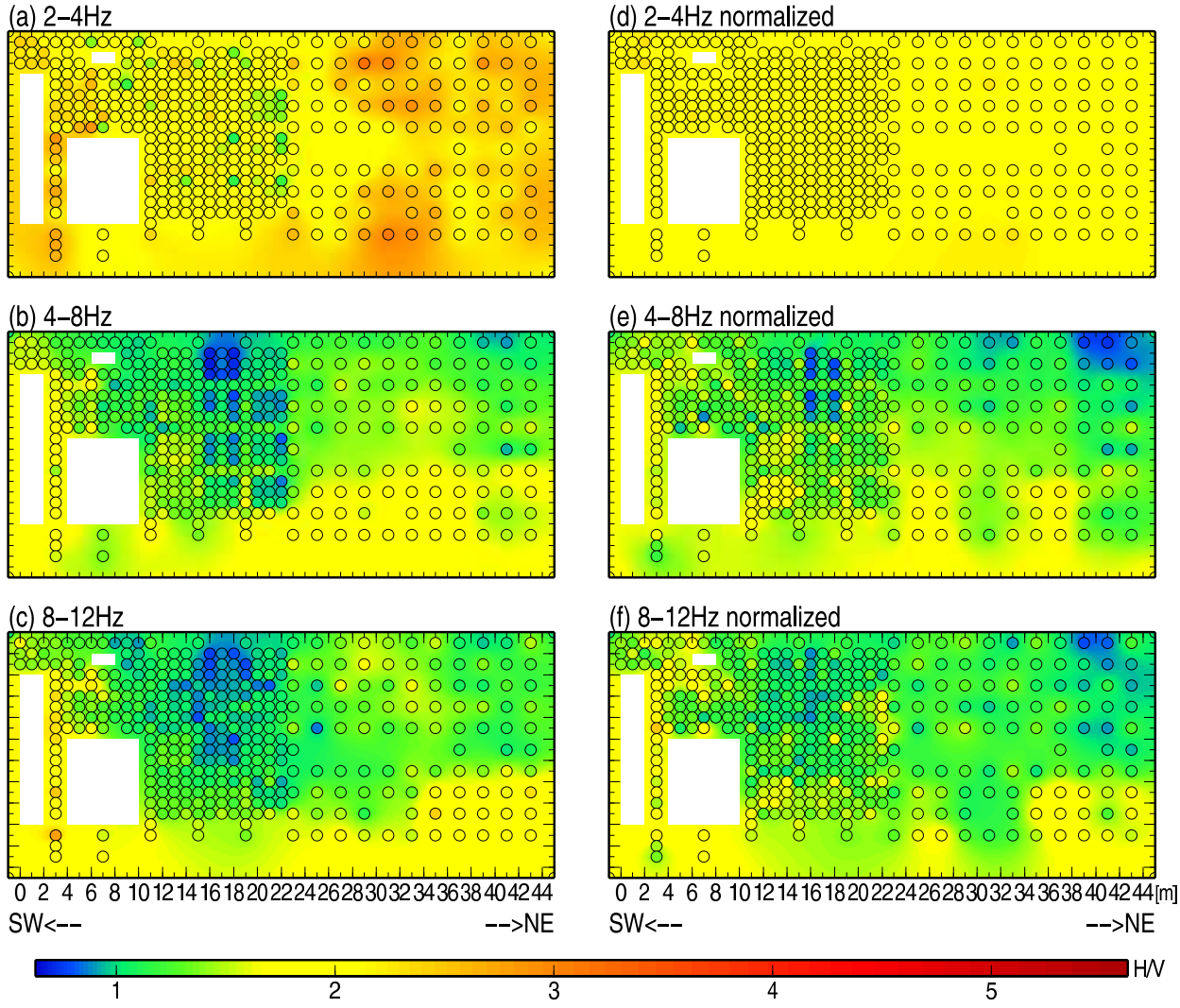

Figure 5: Spatial distribution of the H/V spectral amplitudes for different frequencies. Medians of H/V spectra at (a)(d) 2-4, (b)(e) 4-8, and (c)(f) 8-12 Hz are shown in the left side. Figures (d)-(f) are normalized by the median at 2-4 Hz.

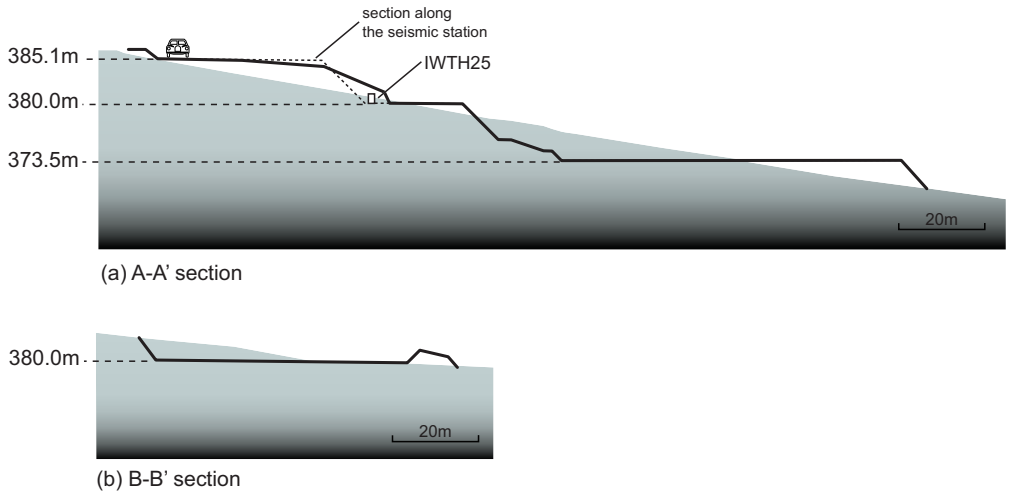

Figure 6: Section around station IWTH25. The gray area shows the ground height prior to leveling, and the solid black line shows the ground height after leveling. The vertical scale is twice as large as the horizontal one (i.e. VE=2:1). The section lines are shown in Figure 2.

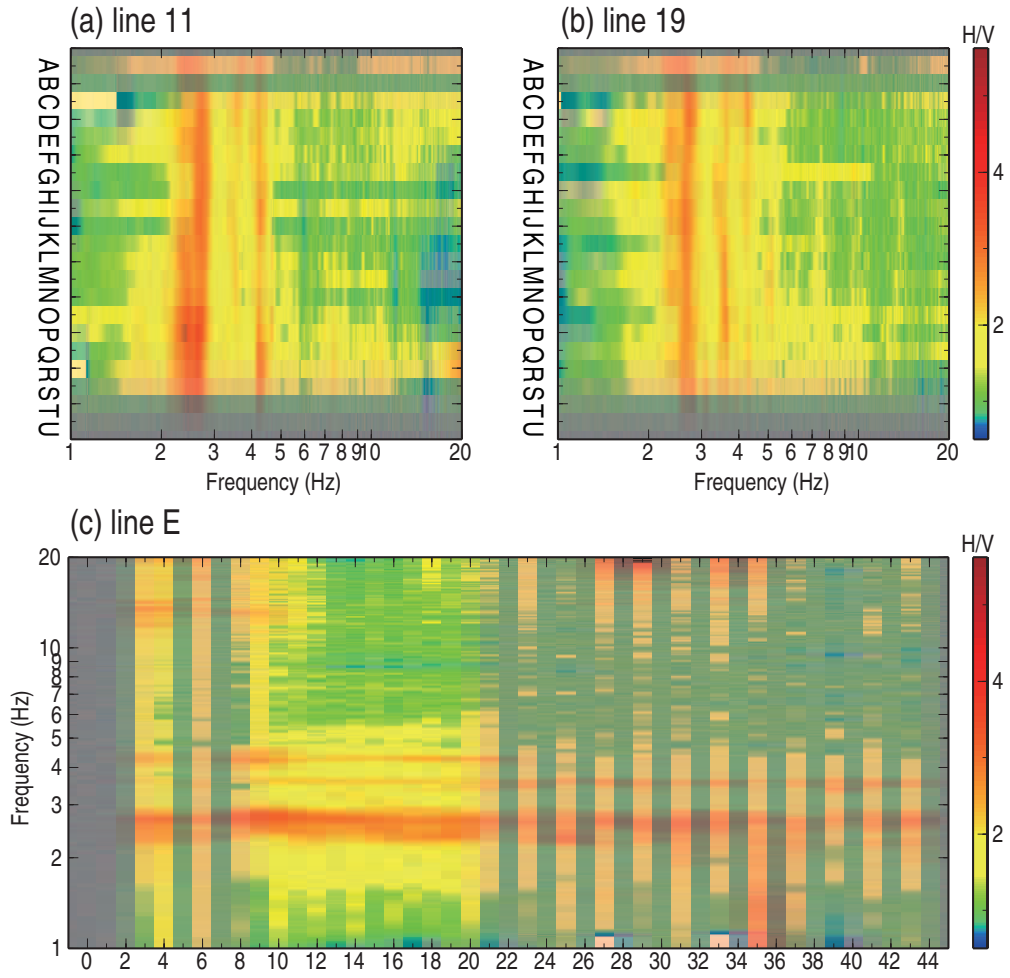

Figure 7: H/V spectra along the (a) line 11, (b) line 19, and (c) line E.

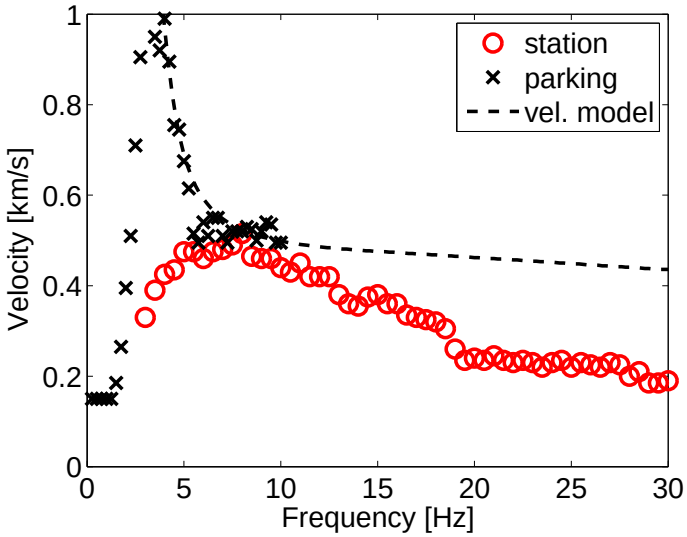

Figure 8: Dispersion curves at the station level (circles) and parking level (crosses). The dashed line shows the dispersion curve corresponding to the PS logging data.

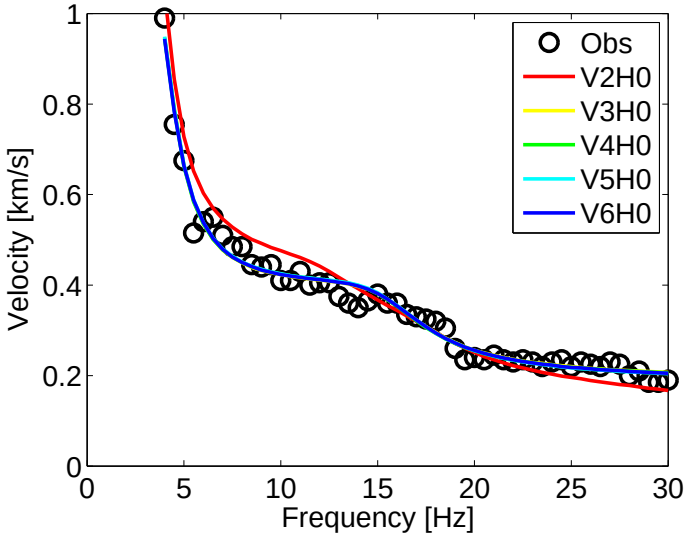

Figure 9: Dispersion curves for models with different numbers of parameters V_s. The curves for models V3H0, V4H0, V5H0 and V6H0 overlap.

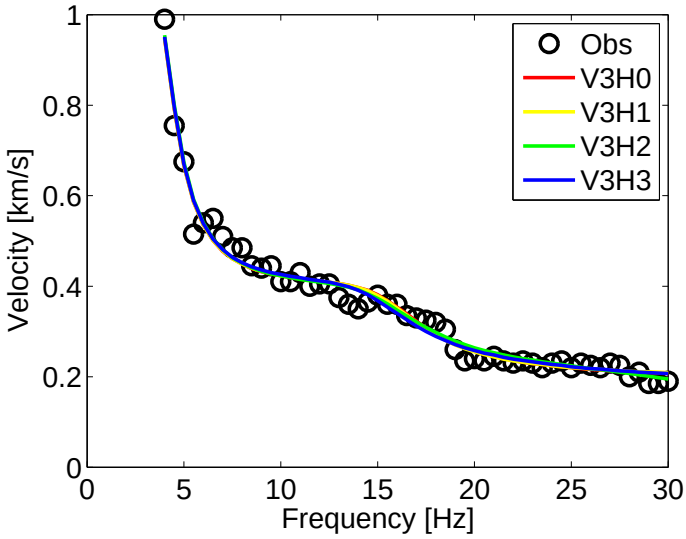

Figure 10: Dispersion curves for models with different numbers of parameters H. The curves for models V3H0, V3H1, V3H2, and V3H3 overlap.